

# Efficient and Stable Inverted Perovskite Solar Cells Incorporating Secondary Amines

Hao Chen, Qi Wei, Makhsud I. Saidaminov, Fei Wang, Andrew Johnston, Yi Hou, Zijian Peng, Kaimin Xu, Wenjia Zhou, Zhenghao Liu, Lu Qiao, Xiao Wang, Siwen Xu, Jiangyu Li, Run Long, Youqi Ke, Edward H. Sargent,\* and Zhijun Ning\*

Large-bandgap perovskites offer a route to improve the efficiency of energy capture in photovoltaics when employed in the front cell of perovskite–silicon tandems. Implementing perovskites as the front cell requires an inverted (p–i–n) architecture; this architecture is particularly effective at harnessing high-energy photons and is compatible with ionic-dopant-free transport layers. Here, a power conversion efficiency of 21.6% is reported, the highest among inverted perovskite solar cells (PSCs). Only by introducing a secondary amine into the perovskite structure to form  $\text{MA}_{1-x}\text{DMA}_x\text{PbI}_3$  (MA is methylamine and DMA is dimethylamine) are defect density and carrier recombination suppressed to enable record performance. It is also found that the controlled inclusion of DMA increases the hydrophobicity and stability of films in ambient operating conditions: encapsulated devices maintain over 80% of their efficiency following 800 h of operation at the maximum power point, 30 times longer than reported in the best prior inverted PSCs. The unencapsulated devices show record operational stability in ambient air among PSCs.

Low-cost and high-efficiency solar cells are attractive candidates to meet the growing demand for renewable energy. Silicon solar cells have reached a power conversion efficiency (PCE) of 26.6%,<sup>[1]</sup> approaching their theoretical limit; tandem solar cells offer a means to improve further the efficiency of solar cells.

In a tandem solar cell, two cells stacked mechanically<sup>[2–4]</sup> or monolithically<sup>[5,6]</sup> generate a total power that exceeds what each subcell can generate individually. Perovskites represent a particularly attractive candidate for pairing with silicon, and silicon:perovskite tandem solar cells have demonstrated a total PCE of 28%.<sup>[7]</sup>

When constructing tandem solar cells, minimizing parasitic absorption in the window layers through which the light passes before reaching perovskite and silicon absorbers is crucial to reach high efficiency.<sup>[5]</sup> In the most efficient PSCs—which use a normal (n–i–p) architecture—hole transport layers (HTLs) with ionic dopants deposited on top of the perovskite act as a window layer.<sup>[8–10]</sup> These HTLs have parasitic absorption, and they also accelerate the degradation of PSCs as a result of mobile ionic

dopants.<sup>[11]</sup> Perovskite solar cells (PSCs) with an inverted architecture (p–i–n)—in which a transparent and robust electron transporter layer (ETL) is deposited on top of perovskite—are an excellent choice for the fabrication of perovskite:silicon tandems.

H. Chen, Q. Wei, F. Wang, Z. Peng, K. Xu, Dr. W. Zhou,  
X. Wang, S. Xu, Prof. Y. Ke, Prof. Z. Ning  
School of Physical Science and Technology  
ShanghaiTech University  
Shanghai 201210, P. R. China  
E-mail: ningzhj@shanghaitech.edu.cn

H. Chen  
School of Chemistry and Chemical Engineering  
University of Chinese Academy of Science  
Beijing 100049, P. R. China


H. Chen  
Shanghai Institute of Ceramics  
Chinese Academy of Science  
Shanghai 200050, P. R. China

Dr. M. I. Saidaminov, Dr. A. Johnston, Dr. Y. Hou, Prof. E. H. Sargent  
Department of Electrical and Computer Engineering  
University of Toronto  
Toronto, Ontario M5S 3G4, Canada  
E-mail: ted.sargent@utoronto.ca

Dr. Z. Liu, Prof. J. Li  
Shenzhen Key Laboratory of Nanobiomechanics  
Shenzhen Institutes of Advanced Technology  
Chinese Academy of Sciences  
Shenzhen 518055, Guangdong, P. R. China

L. Qiao, Prof. R. Long  
College of Chemistry  
Key Laboratory of Theoretical & Computational  
Photochemistry of Ministry of Education  
Beijing Normal University  
Beijing 100875, P. R. China

Prof. J. Li  
Department of Mechanical Engineering  
University of Washington  
Seattle, WA 98195-2600, USA

 The ORCID identification number(s) for the author(s) of this article can be found under <https://doi.org/10.1002/adma.201903559>.

DOI: 10.1002/adma.201903559

Unfortunately, state-of-art-inverted PSCs with inorganic HTLs suffer from low efficiency: the highest certified PCE of inverted PSCs is 19.2%,<sup>[12]</sup> fully five absolute power points lower than the best noninverted PSCs.<sup>[7]</sup> Furthermore, the operational stability of efficient inverted PSCs has, until now, been less than 20 h under continuous operation.<sup>[13]</sup>

To investigate inverted PSCs, we began with molecular dynamic simulations of the lattice dynamics of MAPbI<sub>3</sub> (MA is methylamine) perovskite on a NiO surface: we observed that the lattice mismatch results in structural disorder at the interface. This favors the formation of interface defects which result in carrier recombination at the interface. To reduce interfacial defects, we introduced a secondary amine, dimethylamine (DMA), to partially replace methylamine (MA) in the perovskite structure. The addition of DMA increases the rigidity of the perovskite structure and improves the lattice match, thereby reducing lattice disorder at the perovskite/NiO interface and suppressing the formation of defects.

We then fabricated inverted PSCs in which the HTL is inorganic NiO; as a result of the DMA incorporation, the optimized devices show an in-lab PCE of 21.6% and an externally certified efficiency of 20.8%. In addition, the secondary amine weakens the hydrogen bonding between the perovskite active layer and ambient water, increasing the stability of PSCs. The encapsulated inverted PSCs retain over 80% of their initial efficiency after 800 h of continuous maximum power point (MPP) operation.

We performed density function theory (DFT) calculations and first-principles adiabatic molecular dynamics (MD) simulations to calculate the structure and properties of DMA-based perovskites.<sup>[14]</sup> The average length of I–Pb bonds in MA1 (MAPbI<sub>3</sub>) and DMA0.125 (MA<sub>0.875</sub>DMA<sub>0.125</sub>PbI<sub>3</sub>) at 0 and 300 K were calculated (Figure 1a and Figure S1, Supporting Information). The change in the bond length due to thermal expansion in DMA0.125 (0.091 Å) is notably smaller than that of MA1 (0.154 Å) (Figure 1b). In addition, DMA0.125 showed decreased canonically averaged standard deviation of the position of I and Pb atoms, indicating that DMA0.125 is more rigid than MA1 (Table S1, Supporting Information).

Ab initio molecular dynamics (AIMD) were simulated to compare the NiO (001)/MA1 (110) interface and the NiO (001)/DMA0.125 (100) interface. As shown in Figure 1f,g, once we allow the MD trajectory to progress for 5 ps, we find that the NiO (001)/MA1 (110) interface becomes significantly more disordered than the NiO (001)/DMA0.125 (100) interface. The highest occupied (HOMO) and lowest unoccupied (LUMO) molecular orbitals show that the states are more localized on the interface of NiO (001) and MA1 (110), indicating an increased defect density. To quantify the difference, we also calculated the radial distribution function (RDF) for the two structures. Both Pb–I and Ni–O RDFs in DMA0.125 show a higher and narrower peak (Figure S2, Supporting Information), also consistent with reduced disorder at the NiO (001)/DMA0.125 (100) interface.

We then analyzed the influence of structural stiffness on the formation energy of defects (Figure 1c and Figure S3, Supporting Information): PbI<sub>2</sub> vacancies, MAI vacancies, and antisite Pb<sub>i</sub> defects. These have been reported to lead to perovskite degradation via vacancy-assisted decomposition.<sup>[15]</sup> The formation energies of the aforementioned defects in DMA0.11

are all higher than those of MA1 (Figure 1d and Table S2, Supporting Information), resulting in a lower defect density in DMA0.11. This is consistent with the interface defect simulation-based studies reported above.

MA<sub>1-x</sub>DMA<sub>x</sub>PbI<sub>3</sub> perovskite films were prepared via a one-step spin-coating method<sup>[16,17]</sup> (see the Experimental Section for details) by varying the ratio of DMA:MA in the precursor solution. DMA content in the final films determined by <sup>1</sup>H NMR agrees with that in the starting precursor solutions (Figure S4, Supporting Information). The amount of DMA present in the final films is precisely controlled, ensuring that the perovskite tolerance factor is obeyed; we believe that this is important, since uncontrolled DMA content has been associated with low PCE exhibited in previous DMA-incorporating perovskites.<sup>[18,19]</sup>

We characterized the crystal structure of films with X-ray diffraction (XRD; Figure 2a,b). MA1 and DMA0.03 show two dominant diffraction peaks at 2θ of 14.1° and 28.4°, corresponding to (110) and (210) planes of tetragonal perovskite phase, respectively. As we increased the DMA:MA ratio, we observed a gradual shift of the peaks of (110) and (210) planes occur (Figure 2b), indicating phase transformation from tetragonal to cubic (Table S3, Supporting Information). When the fraction of DMA is higher than 0.3, we observed phase segregation, i.e., co-formation of 3D perovskite and 1D hexagonal DMAPbI<sub>3</sub>.<sup>[20–22]</sup>

We then characterized optical properties of the samples (Figure 2c). No obvious change in the absorption spectra for *x* < 0.3 (Figure S7a, Supporting Information) indicates that the DMA has negligible impact on the electronic structure. The photoluminescence (PL) intensity of the optimized DMA doped film is ≈2× higher than that of MA1. The PL decay lifetime of the DMA0.11 film is 35 ns, much longer than that of MA1 (19 ns) (Figure 2d and Table S4, Supporting Information). The longer PL lifetime along with the higher steady-state PL of DMA0.11 indicates that the nonradiative recombination is reduced in the DMA-incorporating films, suggesting that the trap state density is reduced.<sup>[23]</sup> This is consistent with the higher formation energy of the perovskite structure obtained in DFT studies.

We used electrochemical strain microscopy (ESM) to map the structural stability of films.<sup>[24]</sup> Perovskite grains are clearly observed in the image (Figure S10, Supporting Information). We then investigated the ionic migration rate at grains and grain boundaries using a relaxation technique<sup>[25]</sup> under a step-wise DC bias (Figure 3a,b and Figure S9, Supporting Information). The DC bias modifies the local ion distribution beneath the probe; when it is removed, the transient response enables an estimation of the ions' diffusion rate. The relaxation times of DMA0.11 (0.55 s for grains and 0.33 s for grain boundaries) are 50% larger than that of MA1 (0.34 s for grains and 0.19 s for grain boundaries), indicating inhibited ion diffusion in DMA0.11 (Table S5, Supporting Information).

To investigate the stability of perovskites, we aged perovskites under relative humidity (RH) of 80 ± 5% and tracked the evolution of the absorption spectra for over 10 days (Figure S11, Supporting Information). MA1's optical density at 750 nm decreased to 80% of its original value over this period. In contrast, the DMA0.11 film shows no obvious decrease. We attribute the improved stability to the increased hydrophobicity

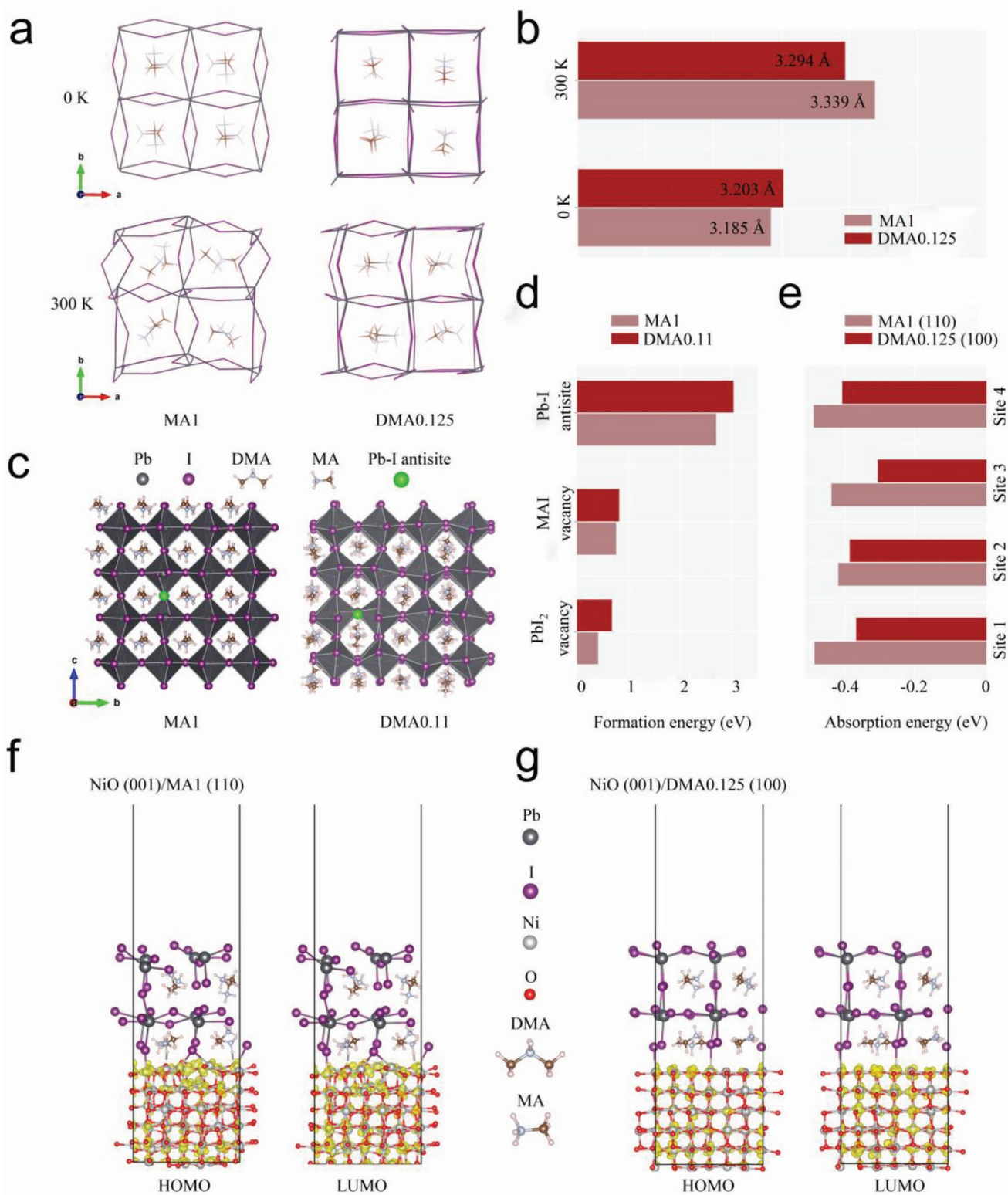


**Figure 1.** DFT calculation and AIMD of NiO–perovskite interfaces. a) Schematic of stiffness changes in different temperature for **MA1** (left) and **DMA0.125** (right) structure. b) Average Pb–I bond length changes of **MA1** and **DMA0.125** structure in different temperature. The smaller variation of bond length for **DMA0.125** means **DMA0.125** structure is stiffer than **MA1** structure. c) Structure configurations used in DFT calculations of Pb–I antisite formation energy. d) The formation energies of antisite and vacancies in **MA1** and **DMA0.11** perovskites. e) The adsorption energies of water on different sites of **MA1** and **DMA0.125** structure. f, g) Interface structures after 5 ps MD simulation and corresponding HOMO and LUMO for NiO (001)/**MA1** (110) (f) and NiO (001)/**DMA0.125** (100) (g). For simplifying the calculation, **MA1** and **DMA0.125** perovskite supercells were used for MD simulation.

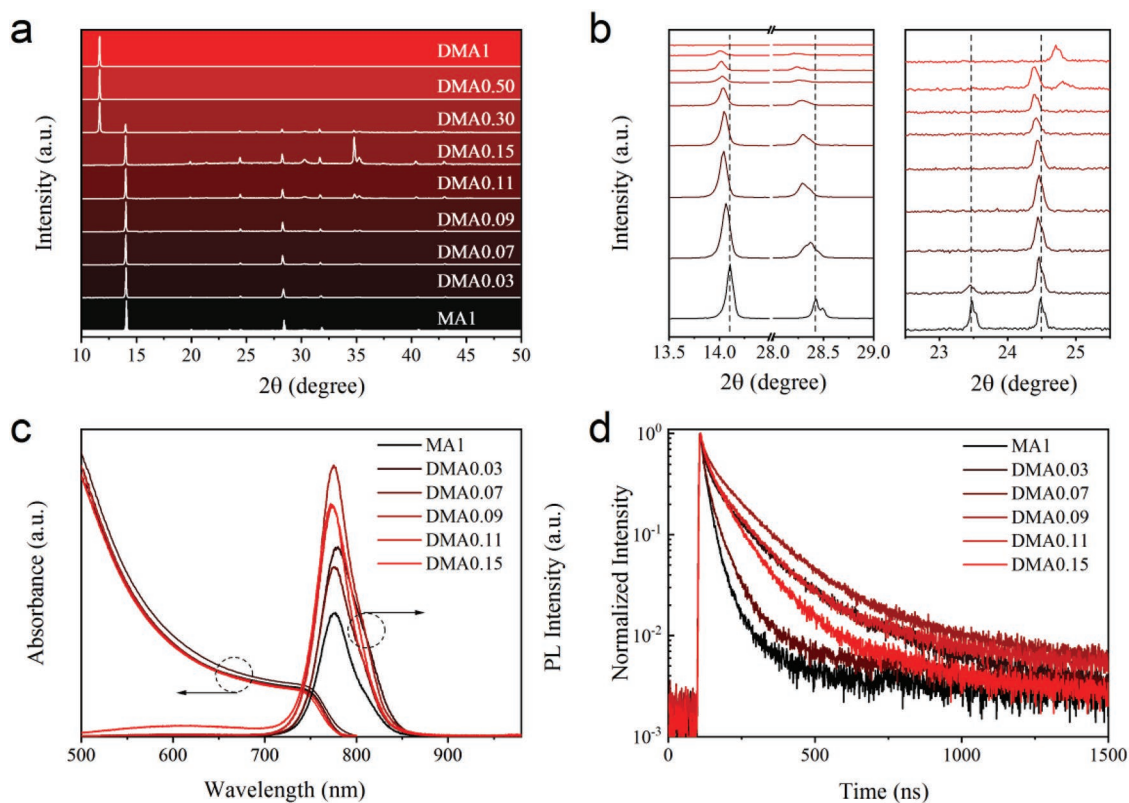


**Figure 2.** Characterization of perovskite films. a) Normalized XRD spectra for the mixed MA/DMA perovskite films containing different percentages of DMA. b) Magnification of the XRD peaks on variation of the DMA content. c) UV-vis absorption and PL spectra of  $\text{DMA}_x\text{MA}_{1-x}\text{PbI}_3$  perovskite films. d) The TRPL spectroscopy of the perovskite films.

of **DMA0.11** films, as confirmed by higher static water contact angle (Figure 3c).

To understand the increased hydrophobicity of **DMA0.11**, we simulated the interaction of a water molecule with the tetragonal **MA1** (110) surface and cubic **DMA0.125** (100) surface (Figure S13, Supporting Information), the most stable lattice planes and the growth orientation for films on  $\text{NiO}_x$  substrates. The representative water adsorption energy for **MA1** and **DMA0.125** are  $-0.49$  and  $-0.37$  eV, respectively. The distance between the water molecule and the surface of the Pb-I lattice was noticeably reduced in **MA1** ( $d = 3.54$  Å) compared to **DMA0.125** ( $d = 4.94$  Å) at this site, and similar trends were found for the other three sites (Figure 3d and Table S6, Supporting Information). This points to increased hydrophobicity in the **DMA0.125** films.

We then used  $\text{MA}_{1-x}\text{DMA}_x\text{PbI}_3$  ( $x$  value from 0% to 15%) perovskite films as the active material for solar cells in a planar inverted architecture indium tin oxide (ITO)/ $\text{NiO}_x$ / $\text{MA}_{1-x}\text{DMA}_x\text{PbI}_3$ /choline chloride/ $\text{C}_{60}$ /bathocuproine (BCP)/Ag (Figure 4a). Here,  $\text{NiO}_x$  (30 nm) and  $\text{C}_{60}$  (23 nm) serve as HTL and ETL, respectively, and a thin choline chloride layer serves as the passivation layer<sup>[26]</sup> on a 450 nm thick perovskite layer (Figure 4b).

We found that the efficiency of solar cells peaks at a DMA fraction of 0.11 (Table 1), showing an optimized PCE of 21.6%, while devices based on **MA1** have a PCE of only 18.2%. The hysteresis index<sup>[27]</sup> value is reduced for **DMA0.11** (Table 2), likely due to the reduction in the rate of ion migration.<sup>[28]</sup> The

integrated  $J_{sc}$  from external quantum efficiency (EQE) measurements for **MA1** and **DMA0.11** are 21.5 and 22.6  $\text{mA cm}^{-2}$  (Figure 4f), respectively, which agree well with the values seen in  $J-V$  curves.

We fabricated dozens of **MA1** and **DMA0.11** perovskite devices. The average PCE of **DMA0.11**- and **MA1**-based devices are 20.5% and 17.4%, respectively (Figure 4d). The stabilized PCE of 21.1% for **DMA0.11** measured at MPP ( $V_{mpp}$ ) is consistent with the value from current  $J-V$  sweeps (Figure 4e). We summarize the PCE of PSCs using the  $\text{NiO}_x$ -based inverted structure (Table S9, Supporting Information); 21.6%, to the best of our knowledge, is the highest efficiency reported to date. We sent a device for independent certification and obtained a certified PCE of 20.8% ( $V_{oc} = 1.138$  V,  $J_{sc} = 21.8$   $\text{mA cm}^{-2}$ , and  $FF = 83.8$  %) (Figure S19, Supporting Information).

To analyze the mechanism for the enhanced efficiency of the  $\text{MA}_{1-x}\text{DMA}_x\text{PbI}_3$ , we studied the electronic properties of the films. Due to the high defect concentration of  $\text{NiO}_x$ , devices employing  $\text{NiO}_x$  layers as an HTL typically exhibit significant carrier recombination at the interface.<sup>[29]</sup> We used dark current and electrochemical impedance spectroscopy (EIS) under dark conditions to evaluate the charge carrier recombination resistance ( $R_{rec}$ ) of the devices. A semicircle in the intermediate-frequency region is associated with charge recombination at interfaces<sup>[30]</sup> between the active layer and  $\text{NiO}_x$ . The larger arc of this semicircle for the **DMA0.11** device (Figure 5b) indicates a large recombination resistance, consistent with the view that car-

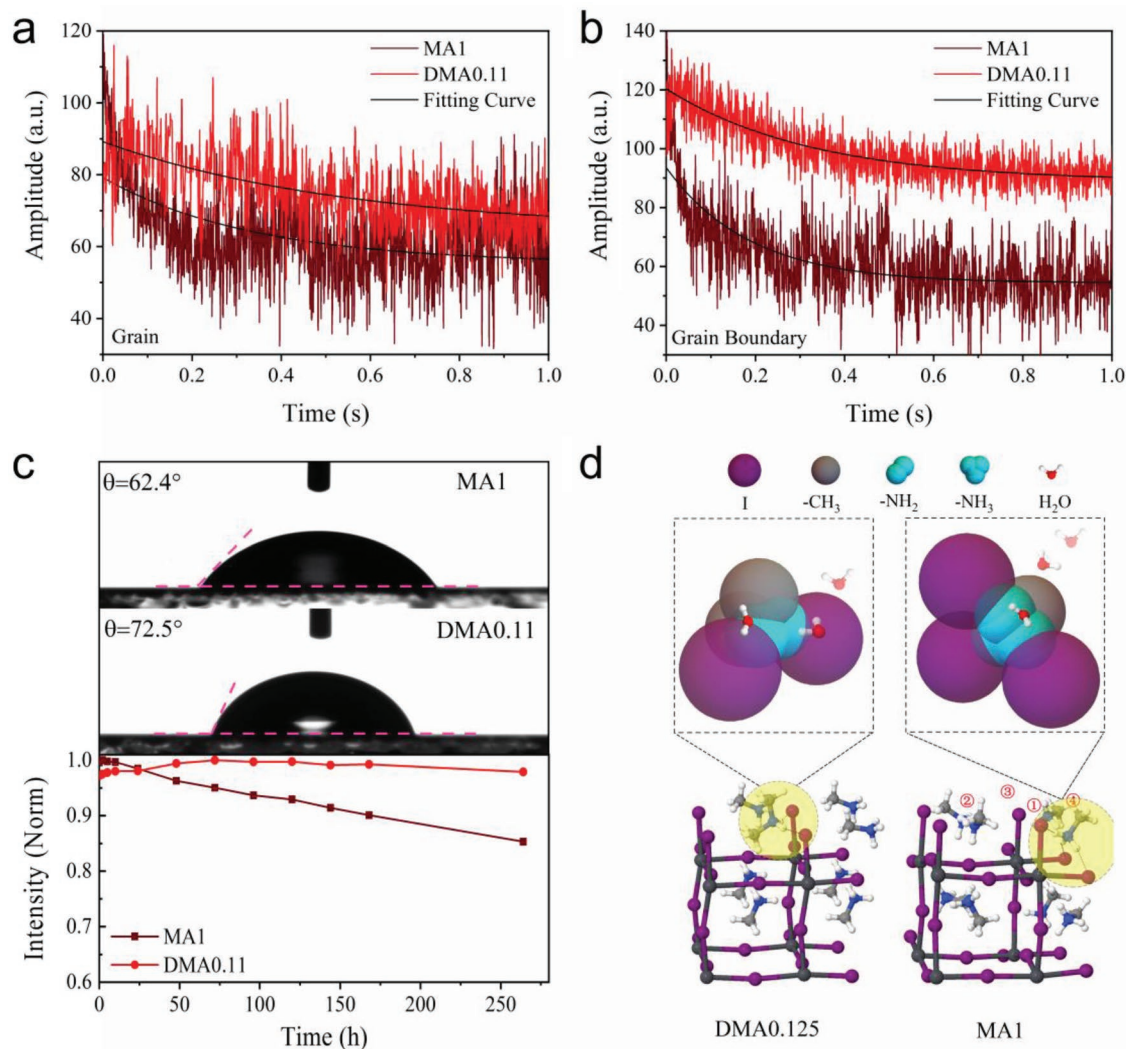


**Figure 3.** ESM relaxation studies and stability characterization of perovskite films on ITO/NiO<sub>x</sub> substrate. a,b) The experimental ESM amplitude of grain (a) and grain boundary (b) versus time for **MA1** and **DMA0.11** measured on ITO/NiO<sub>x</sub>/perovskite under  $-2$  V bias, the time of the x-axis is a reference time. c) The static water contact angle measurement of **MA1** and **DMA0.11** perovskite films and normalized light absorption intensities at 750 nm of the corresponding perovskite films deposited onto NiO<sub>x</sub> substrate exposed at RH  $\approx$  80% as a function of time. d) Water adsorption structure and adsorption model for **DMA0.125** and DMA molecule (left) and **MA1** and MA molecule (right). The cyan ball represents the possible water adsorption area for amino group, the purple ball represents the possible water adsorption area for iodine ion which can compete with amino group, and the gray ball represents the area for methyl group to prevent the water molecule. The radii for the cyan, purple, and gray balls are 1.7, 2.6, and 2.1 Å, respectively, corresponding to the distance from the relaxed structure of these groups with water molecule.

rier recombination between NiO<sub>x</sub> and the perovskite is reduced. Additionally, devices based on **DMA0.11** exhibited a lower reverse saturation current and higher rectification ratio, indicating that interface carrier recombination is reduced as well (Figure 5a).<sup>[31]</sup> For devices based on both **MA1** and **DMA0.11**, the  $V_{oc}$  increased monotonically as light intensity is increased. The lower ideality factor of **DMA0.11** (1.58) (1.86) (Figure 5c) indicates that the nonradiative recombination process was suppressed.<sup>[32]</sup>

We simulate the device efficiency as a function of interface defect concentration using solar cell capacitance simulator modeling.<sup>[33–38]</sup> As the interface defect concentration is decreased from  $3 \times 10^{12}$  to  $10^{12}$  cm<sup>-2</sup>, the PCE increases from 18% to 21% (Figure 5d and Figure S20a,b, Supporting Information); a negligible change in device efficiencies is observed

upon changing carrier mobility from  $10^{-3}$  to  $10^{-4}$  cm<sup>2</sup> V<sup>-1</sup> s<sup>-1</sup> (Figure S20c, Supporting Information). This is consistent with the experimental results, further indicating carrier recombination at the interface plays an important role in PCE.

We compared the stability of the solar cells based on both **MA1** and **DMA0.11** in different environments. **MA1** retained over 90% of their initial PCE following continuous MPP testing, without filtering of UV light, for 40 h of operation in a nitrogen atmosphere (Figure S22b, Supporting Information); whereas **DMA0.11** retained its performance for 120 h. Encapsulated **DMA0.11** devices maintained above 81% of its initial performance following 800 h of continuous operation under illumination using UV-filtered light, with testing carried out in air (Figure 5f).

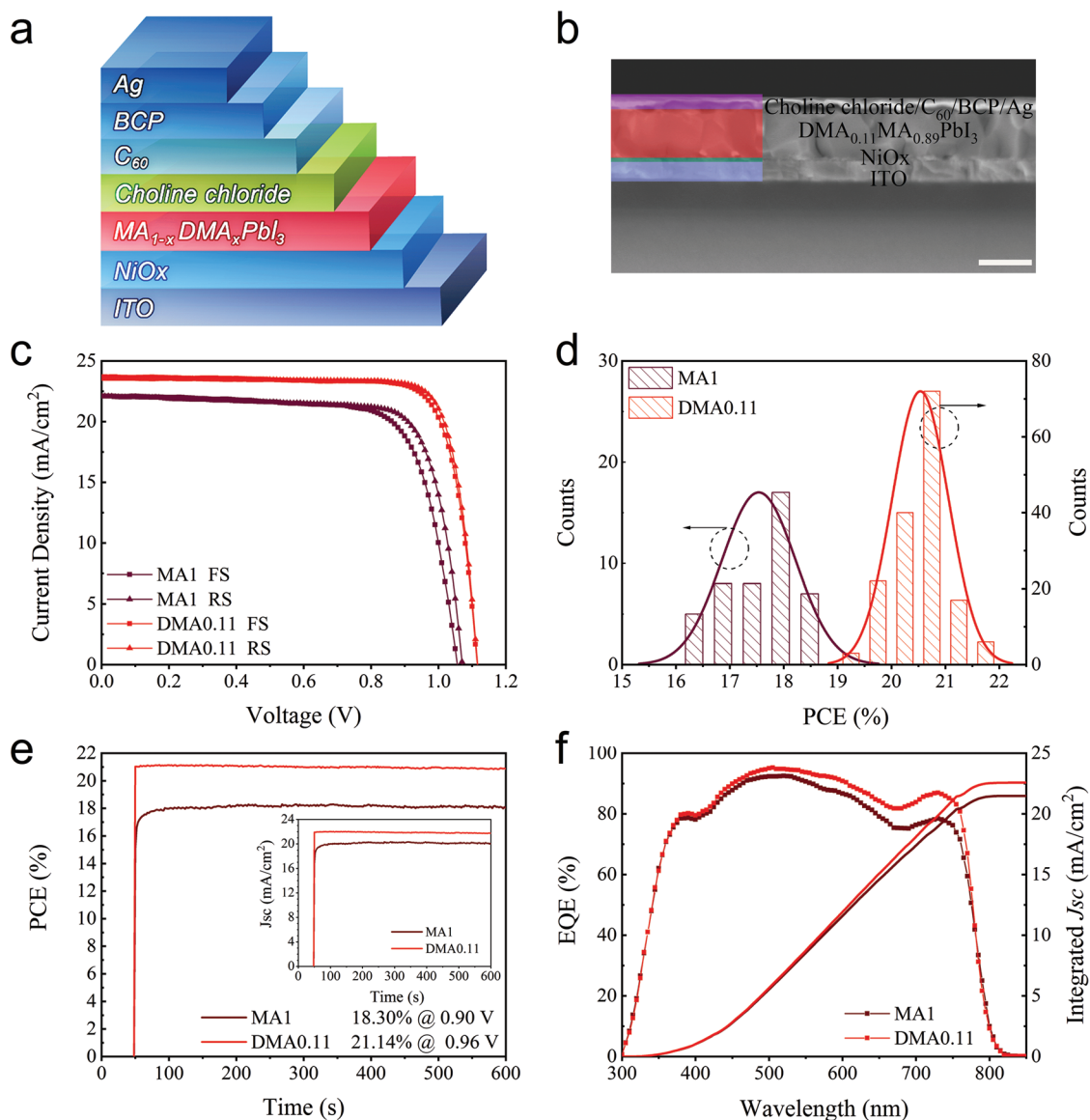


**Figure 4.** Structure and performance of devices. a) Schematic diagram of solar cell configuration. b) Cross-sectional SEM image of the solar cell (scale bar: 500 nm). c)  $J$ - $V$  characteristics from forward scan (FS,  $J_{sc}$  to  $V_{oc}$ ) and reverse scan (RS,  $V_{oc}$  to  $J_{sc}$ ) determined under simulated AM 1.5G illumination for the **MA1** and **DMA0.11** devices. d) Histogram of the PCE values for the **MA1** (45 devices) and **DMA0.11** devices (160 devices). e) Stabilized PCEs of the devices with the inserted photocurrent response spectrum measured at a bias of  $V_{max}$  under 100  $mW\ cm^{-2}$  AM 1.5G irradiation. f) The corresponding incident photon-to-current conversion efficiency spectrum for the **MA1** and **DMA0.11** devices.

Devices based on **DMA0.11** also exhibited enhanced air stability. When storing the devices in an ambient atmosphere with an RH of 65%, the unencapsulated **MA1** devices retained only 20% of their original PCE following 3 days (Figure S22a, Supporting Information); whereas **DMA0.11** retained over 60% of its original PCE after a period of 12 days. We also investigated the photostability of unencapsulated PSCs under MPP operation and continuous illumination in ambient air (RH of 65%): **MA1** cells showed a rapid loss of PCE at a rate of  $-0.34\% \text{ min}^{-1}$  in the linear region;<sup>[15,39]</sup> whereas **DMA0.11** degraded at  $-0.087\% \text{ min}^{-1}$  (Figure 5e). This rate of degradation is slower than the best value ( $-0.1\% \text{ min}^{-1}$ ) reported across PSCs.<sup>[15]</sup> The improved long-term stability for the **DMA0.11**-based devices

can be ascribed to its higher water adsorption energy, as well as lower defect densities.

By introducing the secondary amine molecule DMA, we fabricated quaternary  $MA_{1-x}DMA_xPbI_3$  perovskite films for inverted structure PSCs. Compared to typical  $MAPbI_3$ ,  $MA_{1-x}DMA_xPbI_3$  demonstrated improved crystal rigidity and a lower defect density, particularly at the interface between NiO and perovskite. As a result, DMA-based PSCs showed a PCE of 21.6%, the highest efficiency reported to date, to our knowledge, among inverted PSCs. Due to the increased water repulsion of the secondary amine,  $MA_{1-x}DMA_xPbI_3$ -based solar cells exhibited improved operating stability, retaining 80% of their original efficiency following 800 h of continuous MPP measurement. Unencapsulated

**Table 1.** Photovoltaic parameters of PSCs with different DMA concentrations.

MA <sub>1-x</sub> DMA <sub>x</sub> PbI <sub>3</sub>	V <sub>oc</sub> [V]	J <sub>sc</sub> [mA cm <sup>-2</sup> ]	FF [%]	PCE [%]
MA1	1.062	22.0	78	18.2
DMA0.03	1.060	21.8	80	18.6
DMA0.07	1.104	23.2	82	20.9
DMA0.09	1.112	23.4	82	21.2
DMA0.11	1.116	23.5	82	21.6
DMA0.15	1.109	21.7	82	19.7

Photovoltaic parameters obtained for the best-performing cells containing MA/DMA perovskite systems measured under AM 1.5G Sun illumination.

devices retained 70% of their efficiency following 5 h MPP testing in air. The decay rate of the performance is the lowest among the reported results of all PSCs. The progress herein on inverted structure performance is relevant to silicon/perovskite tandems.

## Experimental Section

**Materials:** Lead iodide (PbI<sub>2</sub>) and BCP were purchased from TCI. Anhydrous dimethylsulfoxide (DMSO), anhydrous dimethylformamide (DMF), anhydrous isopropyl alcohol (IPA), chlorobenzene (CB), and choline chloride were purchased from Sigma Aldrich. Methylammonium iodide (MAI) was purchased from Shanghai MaterWin New Materials Technology Co., Ltd. C<sub>60</sub> was purchased from Xi'an Polymer Light Technology Cory. Aqueous DMA (40% in water) was purchased from Macklin. Hydriodic acid (>45% in water) was purchased from Sinopharm. All salts and solvents were used as received without further purification.

DMAI was synthesized by reacting DMA and hydriodic acid with the volume ratio of 1:1 in an ice bath for 20 min. The white precipitate was recovered by evaporating the reaction mixture at 60 °C for 20 min, then the product was purified twice by recrystallization from IPA solution with diethyl ether. The resulting DMAI was collected by filtration and dried at 60 °C overnight in a vacuum oven.

NiO<sub>x</sub> nanocrystals (NCs) were synthesized according to procedures reported elsewhere, with modifications noted herein below.<sup>[40]</sup> Briefly, 20 mmol Ni(NO<sub>3</sub>)<sub>2</sub>·6H<sub>2</sub>O were dissolved in 20 mL of deionized (DI) water to obtain a dark green solution. Then, 4 mL NaOH solution (10 mol L<sup>-1</sup>) was slowly added into the solution while stirring. After being stirred for 20 min, the colloidal precipitation was thoroughly washed with DI water three times and dried at 80 °C overnight under vacuum. The obtained green powder was then calcined at 270 °C for 2 h to obtain a dark-black powder. The NiO<sub>x</sub> NCs inks were prepared by dispersing the obtained NiO<sub>x</sub> NCs in DI water/IPA (3/1, v/v) with a concentration of 20 mg mL<sup>-1</sup>, stirred for 30 min, then filtered using a 0.22 μm polyethersulfone filter.

**Table 2.** Photovoltaic parameters derived from J–V measurements of different device under forward and reverse scan.

Samples	Scan direction	V <sub>oc</sub> [V]	J <sub>sc</sub> [mA cm <sup>-2</sup> ]	FF [%]	PCE [%]	H-index <sup>a)</sup> [%]
MA1	FS <sup>b)</sup>	1.056	22.1	74	17.3	4.9
	RS <sup>c)</sup>	1.071	22.1	74	18.2	
DMA0.11	FS	1.115	23.7	80	21.2	1.9
	RS	1.116	23.5	82	21.6	

<sup>a)</sup>H-index = (PCE<sub>reverse</sub> – PCE<sub>forward</sub>)/PCE<sub>reverse</sub>; <sup>b)</sup>FS: forward scan; <sup>c)</sup>RS: reverse scan.

**Solar Cell Fabrication:** The patterned ITO substrates were cleaned ultrasonically by sequentially washing with DI water bath with 2% Triton X-100 v/v, DI water, acetone, and IPA for 30 min each. Before using them, the ITO was cleaned via UVO treatment for 20 min. Then, the substrate was spin-coated with a thin layer of NiO<sub>x</sub> NCs film at room temperature without any post-treatment. Stoichiometric precursor solutions were prepared by mixing MAI, DMAI, and PbI<sub>2</sub> in a mixture of DMF and DMSO (4:1 v/v) with MAI/DMAI gradually changing from 1:0 to 0:1, while keeping the PbI<sub>2</sub> molarity equal to 1.30, stirred for 1.0 h at 70 °C, and then filtered with a 0.22 μm poly(tetrafluoroethylene) filter. The perovskite layers were then fabricated by using a one-step spin-coating procedure at 1000 rpm, 10 s, and 4000 rpm, 30 s, respectively. During the second step, 600 μL of toluene was dropped 10 s before the process ended, and this was followed by annealing at 90 °C for 8 min. After this time, the passivation layer (choline chloride) was spin-coated at 4000 rpm for 32 s from an IPA solution (1 mg mL<sup>-1</sup>), then annealed at 90 °C for 10 min. The n-type contact layer was formed by thermally evaporating C<sub>60</sub> (≈20 nm). Then a thin and uniform BCP layer on top of C<sub>60</sub> was deposited by drop-casting BCP dissolved in IPA in 2 to 3 s while spinning the substrate at 6000 rpm. Finally, a 120 nm thick Ag contact was deposited on top of BCP using thermal evaporation under high vacuum (<5 × 10<sup>-7</sup> Torr) in an Angstrom Engineering deposition system. All fabrication steps of perovskite films and top layers were performed in an N<sub>2</sub>-purged glovebox (Vigor Glovebox, O<sub>2</sub> < 0.1 ppm, H<sub>2</sub>O < 0.1 ppm).

**Solar Cell Characterization:** The J–V characteristics of the photovoltaic cells were obtained using a Keithley 2400 Source Meter under simulated one-sun AM 1.5G illumination (100 mW cm<sup>-2</sup>) with a solar simulator (SS-F5-3A, Enli Tech) whose intensity was calibrated with the aid of a certified standard silicon solar cell (SRC-2020, Enli Tech). To avoid stray light, a black mask with an aperture area of 0.04 cm<sup>2</sup> was placed on the surface of devices during measurements. The devices were measured both in reverse scan (1.2 V → -0.1 V, step 0.01 V) and forward scan (-0.1 V → 1.2 V, step 0.01 V); the delay time was 200 ms, and no device preconditioning, such as light soaking or forward voltage bias applied for long time, was applied before starting the measurement. The EQE was measured using a solar-cell-spectra-response measurement system (QE-R, Enli Tech). The Mott–Schottky analysis through capacitance–voltage measurements was collected using an Ivium electrochemical workstation at 1 kHz with the bias potential ranging from 0 to 1 V under dark conditions. The EIS analysis was performed using the Ivium electrochemical workstation at a bias of 0.9 V under dark condition with the frequency ranging from 1 00 000 to 0.01 Hz and amplitude (V) = 0.01. Aging under MPP tracking was carried out on masked devices which were mounted on a temperature-controlled box. The long-term MPP operating aging process was carried out under ambient atmosphere and 1-sun equivalent illumination provided by a white light-emitting diode (LED) light source (420–780 nm). The devices were aged by means of keeping them under maximum load under illumination. The MPP was updated every 60 s by measuring the current response to a small perturbation in potential. Additionally, a full J–V scan was taken every 120 min (at a scan rate of 100 mV s<sup>-1</sup> starting from reverse bias) which was used to extract the displayed parameters for the aging data.

**Other Characterization:** The XRD was measured using a Bruker D8 Advance X-ray diffractometer at room temperature using Cu-Kα radiation (λ = 1.54178 Å) at 40 kV and 40 mA. The scanning electron microscopy (SEM) images were obtained by using a JSM-7800F field-emission scanning electron microscope. The UV–vis absorption spectra were obtained using a Cary Series UV–vis–NIR Spectrophotometer (Agilent Cary 5000). The static PL spectra were obtained using HORIBA FL-3000/RM4-3000 spectrophotometer. The ultraviolet photoelectron spectroscopy (UPS) measurements were carried out with the aid of a Thermo Fisher ESCALAB 250XL; 10 V bias was applied for UPS measurements. Time-resolved PL (TRPL) decay was measured using a Horiba Fluorolog-3 Time-Correlated Single Photon Counting System; the samples were excited using a pulsed laser with a wavelength of 405 nm. NMR measurements were performed using a liquid-state Bruker Avance 500 MHz spectrometer. The ESM experiments were conducted on an Asylum Research MFP-3D AFM using NanoSensors PPP-EFM probes

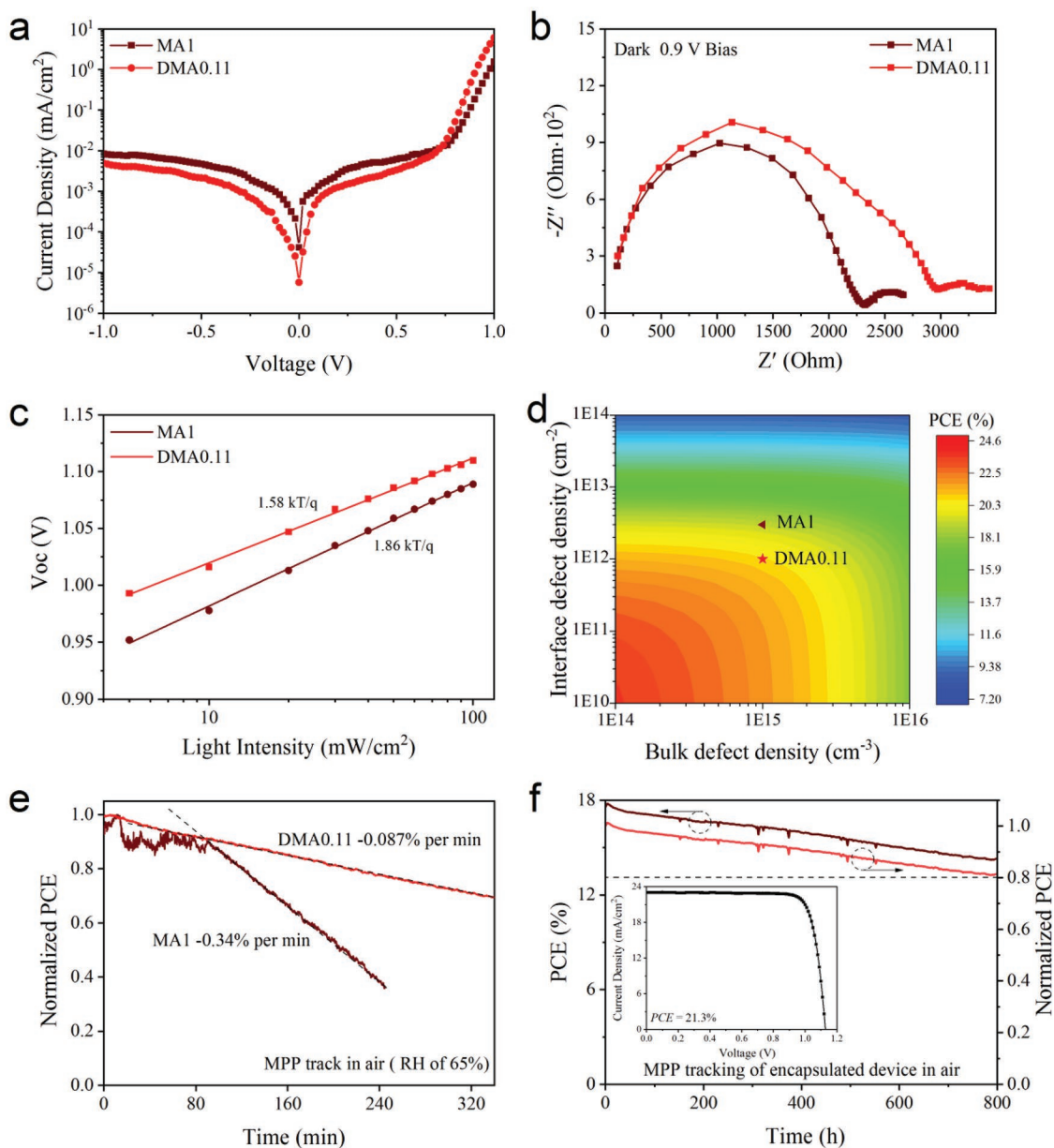


**Figure 5.** Electronic properties and stability of devices. a) Dark  $J$ - $V$  curves for PSCs. b) Nyquist plots of MA1 and DMA0.11 devices under dark condition at bias voltage of 0.9 V. c)  $V_{oc}$  versus light intensity. d) Simulated device performance as the interface defect density is altered. e) Operation of unencapsulated PSCs under MPP conditions with a 420 nm cutoff UV filter in ambient air (relative humidity of 65%). f) MPP tracking of encapsulated DMA0.11 device under continuous LED light illumination at 20 °C and 25% humidity condition. The inset graph is the  $J$ - $V$  curve of the DMA0.11-based device after encapsulation under AM 1.5G light illumination. The initial PCE in tracking curve is about 18% under LED light illumination, lower than the PCE under standard light intensity, because UV light is filtered.

with a PtIr5 metallic coating having tip radius of 25 nm and a nominal resonance frequency of 70 kHz in  $\text{N}_2$ .

**DFT Calculations:** First-principles calculations were performed within the framework of DFT using plane-wave pseudopotential methods as implemented in the Vienna Ab Initio Simulation Package.<sup>[41,42]</sup> The generalized gradient approximation formulated by Perdew, Burke, and Ernzerhof<sup>[43]</sup> was used as the exchange-correlation functional. The cutoff energies for the plane wave basis set used to expand the Kohn-Sham orbitals were 400 eV, and the electron-core interactions were described by the projector augmented wave<sup>[44]</sup> method for the pseudo potentials. For defect formation energy calculation, a  $4 \times 4 \times 4$  supercell of DMA0.11 and the corresponding size supercell of MA1 were constructed to prevent the interactions between defects.

## Supporting Information

Supporting Information is available from the Wiley Online Library or from the author.

## Acknowledgements

The authors acknowledge the Instrument Analysis Center and Electron Microscope Center of ShanghaiTech University. This work was supported by the National Key Research Program (2016YFA0204000), National Science Fund of China (U1632118, 21571129, and 21573022), start-up funding from ShanghaiTech University, Young 1000 Talents



Program, C $\dot{h}$ EM, SPST, ShanghaiTech (Grant 02161943). This publication is based in part on work supported by the US Department of the Navy, Office of Naval Research (Grant Award No.: N00014-17-1-2524). The authors also thank Prof. Qixi Mi, Dr. Zhifang Shi for helpful discussion, and Dr. Xiaoyuan Liu (ShanghaiTech University) for the editing of this manuscript, Huiyan Liu (ShanghaiTech University) for the help of PL characterization, and Yichen He (School of Creativity and Art at ShanghaiTech University), Zhuojia Liu (School of Creativity and Art at ShanghaiTech University) for the help in improving the figures.

## Conflict of Interest

The authors declare no conflict of interest.

## Keywords

defect density, inverted structure, perovskite solar cells, secondary amine, stability

Received: June 4, 2019

Revised: September 2, 2019

Published online:

- [1] K. Yoshikawa, H. Kawasaki, W. Yoshida, T. Irie, K. Konishi, K. Nakano, T. Uto, D. Adachi, M. Kanematsu, H. Uzu, K. Yamamoto, *Nat. Energy* **2017**, *2*, 17032.
- [2] B. Chen, Y. Bai, Z. S. Yu, T. Li, X. P. Zheng, Q. F. Dong, L. Shen, M. Boccard, A. Gruverman, Z. Holman, J. S. Huang, *Adv. Energy Mater.* **2016**, *6*, 1601128.
- [3] T. Duong, Y. L. Wu, H. P. Shen, J. Peng, X. Fu, D. Jacobs, E. C. Wang, T. C. Kho, K. C. Fong, M. Stocks, E. Franklin, A. Blakers, N. Zin, K. McIntosh, W. Li, Y. B. Cheng, T. P. White, K. Weber, K. Catchpole, *Adv. Energy Mater.* **2017**, *7*, 1700228.
- [4] D. W. Zhao, C. L. Wang, Z. N. Song, Y. Yu, C. Chen, X. Z. Zhao, K. Zhu, Y. F. Yan, *ACS Energy Lett.* **2018**, *3*, 305.
- [5] K. A. Bush, A. F. Palmstrom, Z. S. J. Yu, M. Boccard, R. Cheacharoen, J. P. Mailoa, D. P. McMeekin, R. L. Z. Hoye, C. D. Bailie, T. Leijtens, I. M. Peters, M. C. Minichetti, N. Rolston, R. Prasanna, S. Sofia, D. Harwood, W. Ma, F. Moghadam, H. J. Snaith, T. Buonassisi, Z. C. Holman, S. F. Bent, M. D. McGehee, *Nat. Energy* **2017**, *2*, 17009.
- [6] F. Sahli, J. Werner, B. A. Kamino, M. Brauninger, R. Monnard, B. Paviet-Salomon, L. Barraud, L. Ding, J. J. D. Leon, D. Sacchetto, G. Cattaneo, M. Despeisse, M. Boccard, S. Nicolay, Q. Jeangros, B. Niesen, C. Ballif, *Nat. Mater.* **2018**, *17*, 820.
- [7] NREL, Best Research-Cell Efficiencies, <https://www.nrel.gov/pv/assets/pdfs/best-research-cell-efficiencies.20190411.pdf> (accessed: April 2019).
- [8] N. J. Jeon, H. Na, E. H. Jung, T. Y. Yang, Y. G. Lee, G. Kim, H. W. Shin, S. I. Seok, J. Lee, J. Seo, *Nat. Energy* **2018**, *3*, 682.
- [9] W. S. Yang, B. W. Park, E. H. Jung, N. J. Jeon, Y. C. Kim, D. U. Lee, S. S. Shin, J. Seo, E. K. Kim, J. H. Noh, S. I. Seok, *Science* **2017**, *356*, 1376.
- [10] Q. Jiang, Y. Zhao, X. Zhang, X. Yang, Y. Chen, Z. Chu, Q. Ye, X. Li, Z. Yin, J. You, *Nat Photonics* **2019**, *13*, 460.
- [11] Y. Rong, L. Liu, A. Mei, X. Li, H. Han, *Adv. Energy Mater.* **2015**, *5*, 1501066.
- [12] Y. Wu, F. Xie, H. Chen, X. Yang, H. Su, M. Cai, Z. Zhou, T. Noda, L. Han, *Adv. Mater.* **2017**, *29*, 1701073.
- [13] D. Y. Luo, W. Q. Yang, Z. P. Wang, A. Sadhanala, Q. Hu, R. Su, R. Shivanna, G. F. Trindade, J. F. Watts, Z. J. Xu, T. H. Liu, K. Chen, F. J. Ye, P. Wu, L. C. Zhao, J. Wu, Y. G. Tu, Y. F. Zhang, X. Y. Yang, W. Zhang, R. H. Friend, Q. H. Gong, H. J. Snaith, R. Zhu, *Science* **2018**, *360*, 1442.
- [14] J. He, W.-H. Fang, R. Long, O. V. Prezhdo, *ACS Energy Lett.* **2018**, *3*, 2070.
- [15] M. I. Saidaminov, J. Kim, A. Jain, R. Quintero-Bermudez, H. R. Tan, G. K. Long, F. R. Tan, A. Johnston, Y. C. Zhao, O. Voznyy, E. H. Sargent, *Nat. Energy* **2018**, *3*, 648.
- [16] H. S. Kim, C. R. Lee, J. H. Im, K. B. Lee, T. Moehl, A. Marchioro, S. J. Moon, R. Humphry-Baker, J. H. Yum, J. E. Moser, M. Gratzel, N. G. Park, *Sci. Rep.* **2012**, *2*, 591.
- [17] J. H. Heo, S. H. Im, J. H. Noh, T. N. Mandal, C. S. Lim, J. A. Chang, Y. H. Lee, H. J. Kim, A. Sarkar, M. K. Nazeeruddin, M. Gratzel, S. I. Seok, *Nat. Photonics* **2013**, *7*, 486.
- [18] M. V. Lee, S. R. Raga, Y. Kato, M. R. Leyden, L. K. Ono, S. H. Wang, Y. B. Qi, *J. Mater. Res.* **2017**, *32*, 45.
- [19] W. M. J. Franssen, B. J. Bruijnaers, V. H. L. Portengen, A. P. M. Kentgens, *ChemPhysChem* **2018**, *19*, 3107.
- [20] D. Ju, T. Y. Zhao, Y. Y. Dang, G. D. Zhang, X. B. Hu, D. L. Cui, X. T. Tao, *J. Mater. Chem. A* **2017**, *5*, 21919.
- [21] A. Garcia-Fernandez, J. M. Bermudez-Garcia, S. Castro-Garcia, A. L. Llamas-Saiz, R. Artiaga, J. Lopez-Beceiro, S. Hu, W. Ren, A. Stroppa, M. Sanchez-Andujar, M. A. Senaris-Rodriguez, *Inorg. Chem.* **2017**, *56*, 4918.
- [22] A. Mancini, P. Quadrelli, G. Amoroso, C. Milanese, M. Boiocchi, A. Sironi, M. Patrini, G. Guizzetti, L. Malavasi, *J. Solid State Chem.* **2016**, *240*, 55.
- [23] D. J. Kubicki, D. Prochowicz, A. Hofstetter, M. Sasaki, P. Yadav, D. Q. Bi, N. Pellet, J. Lewinski, S. M. Zakeeruddin, M. Gratzel, L. Emsley, *J. Am. Chem. Soc.* **2018**, *140*, 3345.
- [24] J. Li, B. Huang, E. Nasr Esfahani, L. Wei, J. Yao, J. Zhao, W. Chen, *npj Quantum Mater.* **2017**, *2*, 56.
- [25] Q. N. Chen, Y. Y. Liu, Y. M. Liu, S. H. Xie, G. Z. Cao, J. Y. Li, *Appl. Phys. Lett.* **2012**, *101*, 063901.
- [26] X. P. Zheng, B. Chen, J. Dai, Y. J. Fang, Y. Bai, Y. Z. Lin, H. T. Wei, X. C. Zeng, J. S. Huang, *Nat. Energy* **2017**, *2*, 17102.
- [27] P. Liu, W. Wang, S. Liu, H. Yang, Z. Shao, *Adv. Energy Mater.* **2019**, *9*, 1803017.
- [28] S. van Reenen, M. Kemerink, H. J. Snaith, *J. Phys. Chem. Lett.* **2015**, *6*, 3808.
- [29] R. L. Wang, X. Wu, K. M. Xu, W. J. Zhou, Y. Q. Shang, H. Y. Tang, H. Chen, Z. J. Ning, *Adv. Mater.* **2018**, *30*, 1704882.
- [30] X. Hou, S. M. Huang, O. Y. Wei, L. K. Pan, Z. Sun, X. H. Chen, *ACS Appl. Mater. Interfaces* **2017**, *9*, 35200.
- [31] H. Luo, X. H. Lin, X. Hou, L. K. Pan, S. M. Huang, X. H. Chen, *Nano-Micro Lett.* **2017**, *9*, 39.
- [32] W. Q. Wu, Z. B. Yang, P. N. Rudd, Y. C. Shao, X. Z. Dai, H. T. Wei, J. J. Zhao, Y. J. Fang, Q. Wang, Y. Liu, Y. H. Deng, X. Xiao, Y. X. Feng, J. S. Huang, *Sci. Adv.* **2019**, *5*, eaav8925.
- [33] J. Verschraegen, M. Burgelman, *Thin Solid Films* **2007**, *515*, 6276.
- [34] M. Burgelman, P. Nollet, S. Degraeve, *Thin Solid Films* **2000**, *361–362*, 527.
- [35] K. Decock, S. Khelifi, M. Burgelman, *Thin Solid Films* **2011**, *519*, 7481.
- [36] K. Decock, P. Zabierowski, M. Burgelman, *J. Appl. Phys.* **2012**, *111*, 043703.
- [37] M. Burgelman, K. Decock, S. Khelifi, A. Abass, *Thin Solid Films* **2013**, *535*, 296.
- [38] R. Wang, X. Wu, K. Xu, W. Zhou, Y. Shang, H. Tang, H. Chen, Z. Ning, *Adv. Mater.* **2018**, *30*, 1704882.
- [39] K. Domanski, E. A. Alharbi, A. Hagfeldt, M. Gratzel, W. Tress, *Nat. Energy* **2018**, *3*, 61.
- [40] F. Jiang, W. C. H. Choy, X. C. Li, D. Zhang, J. Q. Cheng, *Adv. Mater.* **2015**, *27*, 2930.
- [41] G. Kresse, J. Furthmuller, *Comput. Mater. Sci.* **1996**, *6*, 15.
- [42] G. Kresse, J. Furthmuller, *Phys. Rev. B* **1996**, *54*, 11169.
- [43] J. P. Perdew, K. Burke, M. Ernzerhof, *Phys. Rev. Lett.* **1996**, *77*, 3865.
- [44] P. E. Blochl, *Phys. Rev. B* **1994**, *50*, 17953.